Sustainable Energy & Fuels

ROYAL SOCIETY OF CHEMISTRY

PAPER

View Article Online
View Journal | View Issue

Cite this: *Sustainable Energy Fuels*, 2023, 7, 4967

Synthetic styrene-based bioinspired model of the [FeFe]-hydrogenase active site for electrocatalytic hydrogen evolution†

Afridi Zamader, ‡[ab] Bertrand Reuillard, *[a] Julien Pérard,[a] Laurent Billon, [c] Gustav Berggren *[b] and Vincent Artero [a]

Integration of molecular catalysts inside polymeric scaffolds has gained substantial attention over the past decade, as it provides a path towards generating systems with enhanced stability as well as enzyme-like morphologies and properties. In the context of solar fuels research and chemical energy conversion, this approach has been found to improve both rates and energy efficiencies of a range of catalytic reactions. However, system performance still needs to be improved to reach technologically relevant currents and stability, parameters that are heavily influenced by the nature of the incorporated molecular catalyst. Here, we have focused on the integration of a biomimetic $\{Fe_2(\mu\text{-adt})(CO)_6\}$ ($-CH_2NHCH_2S-$, azadithiolate or adt^{2-}) based active site ("$[2Fe2S]^{adt}$"), inspired by the catalytic cofactor of [FeFe] hydrogenases, within a synthetic polymeric scaffold using free radical polymerization. The resulting metallopolymers $[2Fe2S]^{adt}{}_k[DMAEMA]_l[PyBMA]_m$ (DMAEMA = dimethylaminoethyl methacrylate as water soluble monomer; PyBMA = 4-(pyren-1-yl)-butyl methacrylate as hydrophobic anchor for heterogenization) were found to be active for electrochemical H_2 production in neutral aqueous media. The pyrene content was varied to optimize durability and activity. Following immobilization on multiwalled carbon nanotubes (MWNT) the most active metallopolymer, containing ~2.3 mol% of PyBMA, could reach a turnover number for hydrogen production (TON_{H_2}) of $\sim 0.4 \times 10^5$ over 20 hours of electrolysis at an overpotential of 0.49 V, two orders of magnitude higher than the isolated catalyst counterpart. The study provides a synthetic methodology for incorporating catalytic units featuring second coordination sphere functional groups, and highlights the benefit of the confinement within the polymer matrix for catalytic performance.

Received 27th March 2023
Accepted 30th July 2023

DOI: 10.1039/d3se00409k

rsc.li/sustainable-energy

Introduction

Water electrolysis powered by renewable energy is one of the most sustainable methods to produce clean H_2.[1] Current electrolyzer technologies still rely on the use of expensive platinum-group metals (PGMs) based cathodes for proton reduction.[2–4] In order to overcome this issue, the development of efficient noble-metal free H_2 production catalysts is required.[5,6]

In nature, [FeFe]-hydrogenase enzymes are capable of H_2 production at high catalytic rates ($\sim 10^4$ moles of H_2 per mole of enzyme per second) with negligible overpotential requirement at neutral pH using only earth-abundant metals.[7] Their remarkable activities are enabled by a hexa-nuclear iron cofactor denoted the "H-cluster".[8] The latter consists of a [4Fe–4S] cluster, coupled to a diiron active site ($[2Fe]_H$) where the catalysis takes place. The Fe ions of $[2Fe]_H$ are each coordinated by one terminal CO ligand and one terminal CN^- ligand, and a third CO ligand bridges the two ions.[9] The two Fe ions in $[2Fe]_H$ are further bridged by an azadithiolate ($-SCH_2NHCH_2S-$, adt^{2-}) ligand, in which the bridgehead amine is critical for efficient proton delivery during catalysis.[10–13] In recent years, these fascinating biomolecules have been extensively studied on electrode surfaces and their potential application in "bio-hybrid devices" investigated.[14–16] In parallel, [FeFe]-hydrogenases have served as blueprints for the development of molecular bioinspired catalysts.[7,17–22] In particular, extensive efforts have been invested in $[2Fe]_H$ models of the general structure $\{Fe_2(\mu\text{-SR})_2(CO)_6\}$ (RS^- = thiolate ligand).[7,23] Nevertheless, few catalysts in this di-iron family have been reported to display substantial activities when heterogenized on electrodes or incorporated within synthetic macromolecular chains mimicking proteins. A wide range of strategies have been

[a]*Univ Grenoble Alpes, CNRS, CEA, IRIG, Laboratoire de Chimie et Biologie des Métaux, 17 rue des Martyrs, 38000 Grenoble, France. E-mail: bertrand.reuillard@cea.fr*

[b]*Department of Chemistry – Ångström Laboratory, Uppsala University, Box 523, SE-75120 Uppsala, Sweden. E-mail: gustav.berggren@kemi.uu.se*

[c]*Universite de Pau et Pays de l'Adour, E2S UPPA, IPREM, Bio-inspired Materials Group: Functionalities & Self-Assembly, 2 avenue Angot, 64053 Pau, France*

† Electronic supplementary information (ESI) available. See DOI: https://doi.org/10.1039/d3se00409k

‡ Current address: Université Paris Cité, Laboratoire d'Electrochimie Moléculaire, CNRS, F-75006, Paris, France.

reported in the literature by Darensbourg *et al.*,[24,25] Talarmin *et al.*,[26] Artero *et al.*,[27] Pickett *et al.*,[28] Liu *et al.*[29–31] targeting immobilization at carbon-based or metal electrodes *via* covalent grafting or simple physisorption. However, most of these systems showed rapid loss of activity either following the degradation of the linkage or the active sites. More recently Dey and coworkers reported exceptional improvements in the activity of immobilized $\{Fe_2(\mu\text{-adt})(CO)_6\}$ based complexes,[32–34] following physisorption[32,33,35,36] and covalent grafting[34] on edge plane graphite (EPG) electrodes in aqueous media. However, both strategies yielded relatively low catalyst loadings (lower than 1 nmol cm^{-2}). Recently, our groups demonstrated the simple and efficient immobilization of a pyrene containing naphthalene bridged $\{Fe_2(\mu\text{-}SR_2)(CO)_6\}$ complex on multiwalled carbon nanotubes (MWNT).[37] The presence of pyrene enabled catalyst immobilization through π–π interactions, resulting in a largely improved surface loadings (up to 9.5 nmol cm^{-2}) and excellent stability of the anchoring group on the electrode during electrolysis at neutral pH. However, the latter system displayed moderate activity due to the degradation of the active site during catalysis.[37]

In parallel, the integration of such diiron based complexes within organic polymer scaffolds has emerged as a promising approach to improve their stability and catalytic properties.[38–43] Among such metallopolymers, Brezinski *et al.* reported a striking example with the integration of a naphthalene bridged $\{Fe_2(\mu\text{-}SR)_2(CO)_6\}$ complex inside a poly-(2-(dimethylamino)ethyl methacrylate) (PDMAEMA) polymeric scaffold. The resulting metallopolymer [2Fe2S]-PDMAEMA showed excellent activities at neutral pH under homogeneous conditions.[42,43] These outstanding activities were rationalized by the presence of the PDMAEMA which was proposed to provide not only water solubility but also ensuring efficient proton transfer during catalysis as a polybase. We could further demonstrate that redesigning of the aforementioned metallopolymers to include a pyrene anchoring group, yielding [2Fe2S]-P(DMAEMA-*r*-PyBMA) (PyBMA = 4-(pyren-1-yl)-butyl methacrylate) afforded a system showing high electrocatalytic H_2 production activities at neutral pH once immobilized at MWNT based electrodes.[44] However, the catalytic performance of the latter system was limited by the steady degradation of the diiron catalyst over the course of the electrolysis.

In this study, we explored the possibility of improving the performance of such pyrene containing metallopolymers for electrochemical H_2 production through the re-design of the diiron catalyst "active site". More specifically, we strived to incorporate a potentially more robust catalytic core within the polymer based on previously reported molecular designs,[32,33] and we report the successful integration of a $\{Fe_2(\mu\text{-adt})(CO)_6\}$ based catalyst within a polymer scaffold combining both DMAEMA and PyBMA co-monomer units *via* free radical polymerization using azobisisobutyronitrile (AIBN). To the best of our knowledge, this is the first report of a $\{Fe_2(\mu\text{-adt})(CO)_6\}$ derivative active site successfully incorporated within a multifunctional synthetic macromolecular chain. The resulting original metallopolymers were active for H_2 production at neutral pH (Fig. 1A). The influence of the polymer scaffold was elucidated by comparing the activity of the metallopolymers to that of a molecular pyrene modified isolated analogous diiron catalyst.

2. Results and discussion

2.1. Synthesis and characterization

Efforts to incorporate $[Fe_2(\mu\text{-}SCH_2N(CH_2C_6H_4CHCH_2)CH_2S\text{–})(CO)_6]$ (**1** or $[2Fe2S]^{adt}$) (Fig. 1A) inside a styrene based polymeric scaffolds through reversible addition–fragmentation chain-transfer (RAFT) polymerization have been reported.[45] However, those attempts failed at synthesis stage, possibly due to poor stability of the diiron core under the employed conditions. Thus, we employed a synthetic route proceeding *via* a free radical polymerization reaction in the presence of AIBN without any RAFT reagent. For that, complex **1** and PyBMA, were synthesized following previously reported protocols.[44,45] Subsequently, complex **1**, PyBMA and commercially available DMAEMA were used as co-monomers to synthesize the metallopolymers with AIBN as initiator in toluene at 70 °C for 12 hours (Scheme S1†). The pyrene component ensures efficient binding to MWNT, but can result in unwanted radical termination reactions during polymerisation and impair the hydrophilicity of the polymer.[44] Thus three different metallopolymers *i.e.*, $[2Fe2S]^{adt}{}_k[DMAEMA]_l[PyBMA]_m$ were prepared, denoted **1a**, **1b** and **1c** incorporating different molar equivalents of PyBMA with respect to that of DMAEMA in the feed media (1%, 5% and 10% in **1a**, **1b** and **1c**, respectively, Fig. 1A and Scheme S1†) (see ESI† for details). Here k, l and m represent the molar ratios between $[2Fe2S]^{adt}$, DMAEMA and PyBMA, respectively. As reference, an "isolated" diiron site, denoted as $[2Fe2S]^{adt}$-Py or complex **2**, was synthesized (Scheme S2†). Complex **2** incorporates a pyrene anchoring unit but lacks the polymeric scaffold, allowing us to distinguish the influence of the polymeric framework on the electrocatalysis (Fig. 1A). We note that it is unlikely that the amine from adt^{2-} solely acts as secondary coordination sphere proton shuttle as the latter requires *meta* substitution of the aniline moiety, as reported earlier.[35,46]

The synthesized compounds (*i.e.*, metallopolymers **1a–c** and complex **2**) were characterized using a range of spectroscopic techniques. In all three metallopolymers, the ^1H NMR exhibited peaks between 7.0–7.3 ppm due to the aromatic group present at amine bridgehead of the diiron active site. Compared to spectra collected for complex **1** (Fig. S1†), **1a–c** showed negligible shifts in peak positions which suggest that the polymerization did not cause significant changes in the electronic distribution at the metal center. In addition, **1a–c** showed broad peaks between 7.8–8.4 ppm, characteristic of pyrene, and multiple peaks in the aliphatic region (0–5 ppm), originating from DMAEMA (Fig. S2–S5†). Integration of the previously mentioned signature peaks allowed to calculate the ratio between each co-monomer ($k:l:m$), as shown in Table 1, and estimate the composition of the metallopolymers' backbones. This analysis indicated the presence of ~0.9, ~2.3 and ~6.6 mol% of pyrene in **1a**, **1b** and **1c** respectively (Table 1). As expected, the ^1H NMR spectrum of the complex **2** revealed distinct peaks ranging from 3.5 to 5.5 ppm, 7.2 to 7.9 ppm, 8.0

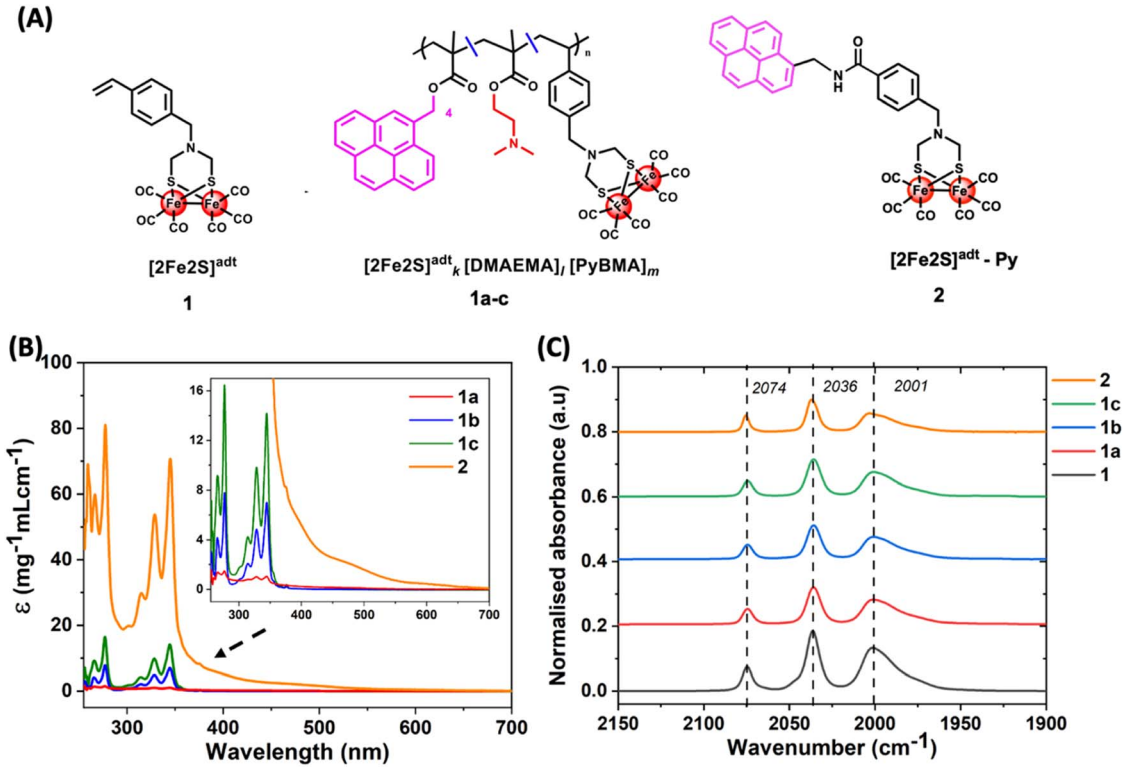

Fig. 1 (A) Schematic representation of synthesized compounds, *i.e.*, complex **1** (synthetic precursor of the metallopolymers), metallopolymer **1a–c** and complex **2**, (B) UV-vis spectra of **1a–c** (197; 50 and 20 μg mL^{-1}) and **2** (11 μg mL^{-1}) in DMF (C) Infrared spectroscopy of **1**, **1a–c** and **2** in $CHCl_3$ using transmission mode. The intensity of FTIR traces of **1a** were multiplied by 3 and **1b** and **1c** multiplied by 10 each to have between comparison with **1** and **2**. Here $k : l : m$ is the ratio of [2Fe2S]^{adt} : [DMAEMA] : [PyBMA]. The exact details of the ratio for each metallopolymers were mentioned in Table 1.

to 8.5 ppm, attributable to the protons present on the aliphatic, bridgehead aromatic and pyrene groups, respectively (Fig. S7†).

UV-vis spectroscopy further supported the presence of the pyrene in both the metallopolymers **1a–c** and complex **2** by showing multiple sharp peaks between 255–355 nm attributed to the pyrene group (Fig. 1B). As the relative pyrene content in **2** is much larger compared to **1a**, **1b** and **1c**, a noticeable enhancement of the intensity of the corresponding pyrene peaks was observed. Infrared spectroscopy allowed to clearly observe the CO stretching bands at 2074, 2036 and 2001 cm^{-1}, confirming the presence of the organometallic active site inside the polymers (Fig. 1C). The peak positions were identical to those observed for complex **1**, again indicating that the polymer had negligible effects on the electronic structure of the di-iron complex, in agreement with the ^{1}H NMR data. Calibrating the absorbance of these infrared bands with that of complex **1** revealed the presence of ~1.6 active sites per mol of **1a** and ~1 active site per mol of both **1b** and **1c** (Fig. S10, S11 and Table S2†). In addition, a strong peak at 1726 cm^{-1} was observed for all polymers, attributable to carbonyls from the ester groups present in the polymeric backbone, as expected this band was not present in the precursor **1** (Fig. S12†).[44] The DMAEMA groups in this type of metallopolymers have been previously shown to have a pK_a of ≈8.4.[43] To further elucidate the protonation chemistry of **1a–c**, the basicity of the adt-amine in the metallo-polymers was probed using **1b** as a representative model, utilizing attenuated total reflection ATR-FTIR spectroscopy. It has been previously reported that below pH 4.4 in

Table 1 Quantitative analysis of all metallopolymers

Metallopolymer or complex	DMAEMA (l)/PyBMA (m)/diiron site (k) final molar ratio[a]	mol% of PyBMA	Fe content[b] (mg$_{Fe}$ g$_{pol}^{-1}$)	M_n[c] (g mol^{-1})	$Đ$[c]
1a	37/0.35/1	0.9	9.6 ± 0.2	14 200	2.7
1b	62/1.5/1	2.3	4.10 ± 0.06	16 650	2.19
1c	53/3.8/1	6.6	4.0 ± 0.1	17 300	2.25
2	—	—	0.16 ± 0.01	—	—

[a] Calculated from ^{1}H NMR spectrum. [b] Measured by ICP-OES. [c] M_n = molecular weight of the metallopolymers and $Đ$ = dispersity, both measured by SEC.

aqueous media, and under strong acidic condition in organic media, the bridgehead amine of Fe(μ-adt)$(CO)_6$ and closely related complexes begin to undergo protonation, resulting in a distinct hypsochromic shift of 20 cm^{-1} in the stretching band of CO ligands coordinated to Fe.[46–48] Interestingly, within the pH range of 2 to 8, no obvious shift of the CO bands is observed, indicating that the bridgehead amine remains in deprotonated state. However, at pH 0, a marginal hypsochromic shift of 3 to 8 cm^{-1} was noticed (Fig. S13†). To identify the origin of the latter shift, a comparative study was carried out using a similar metallopolymer, [2Fe2S]-P(DMAEMA-*r*-PyBMA),[44] where the active site lacks the bridgehead amine. The results revealed that the later metallopolymer exhibited only a minor 1–2 cm^{-1} hypsochromic shift in the CO bands when transitioning from pH 7 to pH 0 (Fig. S14†). This finding suggests that observed shift (3–8 cm^{-1}) for **1b** could be due to the protonation of the bridgehead nitrogen at pH 0, albeit we note that the shift is unusually small.

Complex **2** also exhibited the expected carbonyl ligand bands, with wavenumbers of 2075, 2037, and 2002 cm^{-1} along with a weak carbonyl stretching band at 1659 cm^{-1} attributed to the presence of the amide bond (Fig. 1C and S15† orange trace). Inductively coupled plasma optical emission spectrometry (ICP-OES) was further employed to quantify the concentration of Fe in the polymers and 9.6 ± 0.2 mg of Fe per gram polymer (mg_{Fe} g_{pol}^{-1}) was estimated for **1a** while 4.10 ± 0.06 and 4.0 ± 0.1 mg_{Fe} g_{pol}^{-1} were estimated for **1b** and **1c**, respectively. The discrepancy between the Fe content estimated by NMR relative to the ICP quantification (about 36–55% of expected Fe could be detected in ICP) can be rationalized by the relatively small NMR signals used for the quantification. However, degradation of a small fraction of the Fe–CO core during the polymerization reaction cannot be fully excluded, as previously proposed.[45] Similarly, complex **2** exhibited 0.16 ± 0.01 g of Fe per gram of complex, within the error margin of the expected value (0.15 g of Fe per gram of complex). Size exclusion chromatography (SEC) of metallopolymer **1a–c** showed that the molecular weight varied between 14 200–17 300 g mol^{-1} with dispersity (*Đ*) ranging from 2.2 to 2.7. The dispersity values indicate a degree of length inhomogeneity in the metallopolymers (*i.e.* $Đ > 1$), which can be ascribed to the nature of the employed polymerization method, *i.e.*, free radical polymerization (Fig. S16,† and Table 1). The combination of ICP-OES and SEC data also provides a second measure of active site incorporation, suggesting ~1.2 active sites per mole for **1a** and ~0.6 active sites per mole of both **1b** and **1c**, in line with the estimates from infrared spectroscopy discussed above (Tables 1 and S2†).

2.2. Electrochemical assessments

2.2.1. Homogeneous electrochemistry. The electrochemical properties of the synthetic precursor complex **1**, pyrene modified diiron site complex **2** and metallopolymers **1a–c** were first studied in organic media. Cyclic voltammetry (CV) studies of complex **1** showed a quasi-reversible redox event at $E_{1/2} = -1.55$ V *vs.* $Fc^{+1/0}$ ($E_{p,c} - E_{p,a} = \Delta E_p = 130$ mV) whereas both complex **2** and the metallopolymers displayed an irreversible cathodic wave located at −1.56 V and between −1.62 to −1.65 V *vs.* $Fc^{+1/0}$, respectively (Fig. S17 and S18†). These redox processes were assigned to an Fe based one-electron redox process (Fe^IFe^I/Fe^IFe^0) in agreement with previous reports on closely related diiron active sites.[33,49,50] In contrast to **1** and **2**, **1a–c** are soluble in water due to the presence of DMAEMA units in the conjugated macromolecular chain. Therefore, the electrocatalytic activities of the metallopolymers were further assessed in aqueous media (0.2 M sodium phosphate buffer, pH 7) at a glassy carbon electrode (GCE). Under these conditions, **1a–c** displayed a single irreversible reduction process with an onset potential of −0.34 to −0.36 V *vs.* RHE attributed to the electrocatalytic reduction of protons. Catalytic currents between −1.2 to −2.4 mA cm^{-2} could be reached at −0.65 V *vs.* RHE, with **1a** showing the highest current densities (Fig. 2A and Table 2).

2.2.2. Heterogeneous electrochemistry. Taking advantage of the pyrene anchoring groups, the metallopolymers **1a–c** and complex **2** were then immobilized at the surface of MWNT modified electrodes (**1a–c**/MWNT and **2**/MWNT) following previously reported protocols.[37,44] The loading of electrochemically active $[2Fe2S]^{adt}$ centers at the MWNT electrodes was estimated using data from CV measurements of **1a–c**/MWNT in CH_3CN. **1a–c**/MWNT showed a quasi-reversible reduction event at $E_{1/2} \approx -1.53$ to −1.57 V *vs.* $Fc^{+1/0}$ ($\Delta E_p = 40$–60 mV) similar to that under homogeneous condition, again attributed to a one-electron redox process (*i.e.*, Fe^IFe^I/Fe^IFe^0). The peak current of the latter process was found to vary linearly with scan rate, confirming the grafting of the catalysts (Fig. S21–S23 and Table S3†).[51] Similarly, complex **2** showed a quasi-reversible signal at ≈−1.63 V *vs.* $Fc^{+1/0}$ ($\Delta E_p = 35$ mV) (Fig. S24†). The relative cathodic shift of the redox potentials as compared to homogeneous (organic) conditions is attributed to the difference in employed solvent (DMF *vs.* CH_3CN).[37] A scan rate dependency study was difficult to perform for **2**/MWNT as the catalyst was leaching during CV in organic solvent, where the catalyst is soluble. Integration of the reduction wave allowed to estimate active site loadings of 3.7 ± 0.3, 2.7 ± 0.4, 2.3 ± 0.4 and 13.9 ± 0.6 nmol cm^{-2} for **1a**, **1b**, **1c** and **2**, respectively (Table 2). We note that the observed loading is close to previously reported surface concentrations of electrochemically active metallopolymers of comparable composition and size (Table 2).[44] A complementary estimation of the active site loading was accomplished using ICP-OES which detected diiron active site surface concentrations of 6.80 ± 0.03, 5.4 ± 0.1, 3.8 ± 0.1 and 33.6 ± 5.5 nmol cm^{-2} on MWNT for **1a**, **1b**, **1c** and **2** respectively (Table S4†). Comparing the active site density on electrodes estimated by CV and ICP-OES indicates that only 40–60% of the active sites present on the electrodes could be detected using CV for **1a–c** and **2**/MWNT. The lower loading value measured *via* CV may be explained by the specific behavior of surface-immobilized molecular species depending on their positioning with regards to the electrochemical double layer, as recently highlighted.[52] As the synthesized polymers showcase a rather large size dispersity, it is likely that the environment varies slightly from one catalytic site to another, triggering an inhomogeneous redox response. In addition, this could also be linked to their positioning in the porous MWNT film as it is

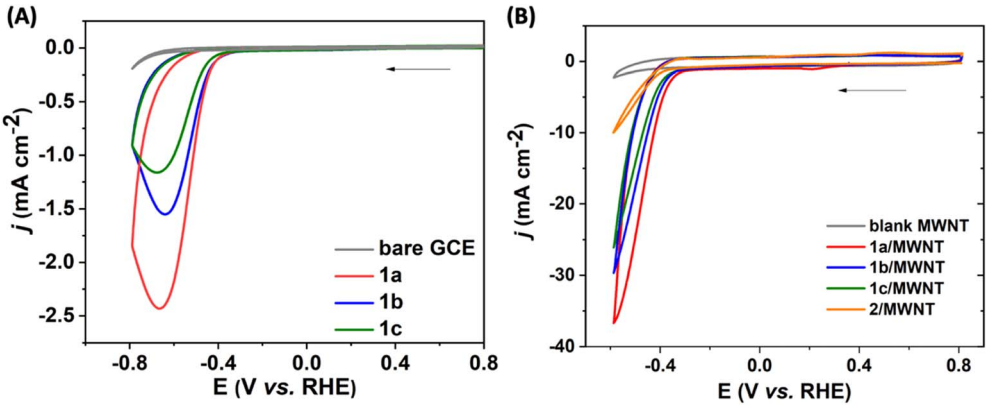

Fig. 2 CV of metallopolymers **1a–c** and complex **2**. (A) Homogeneous conditions with a concentration of 20 μM of **1a–c** at a GCE; (B) heterogeneous condition; following immobilization on MWNT/GCE. The CV measurements were compensated for ohmic drop (85%), in 0.2 M sodium phosphate buffer, pH 7 under argon (ν = 100 mV s^{-1}).

likely that deeply embedded metallopolymers have less access to electrolyte, thus directly impeding their redox response.[53,54] Depending on the interplay between the electrolyte and the metallopolymers, this may result in variations in electrochemical activity and cause poor to silent response in CV experiments.[52] Taken together these data indicate that a variety of active sites are present on our electrodes, including a fraction which is not directly detectable by CV.

The electrocatalytic properties of the modified electrodes were then characterized in 0.2 M phosphate buffer at pH 7. From CV measurements, the **1a–c**/MWNT modified electrodes displayed an onset potential ranging from −0.32 V to −0.33 V *vs.* RHE, and reached high current densities ranging from −24 ± 2 to 36 ± 1 mA cm^{-2} at −0.6 V *vs.* RHE. As observed in homogeneous conditions, the highest currents densities were observed with **1a** followed by **1b** and **1c** (Fig. 2B and Table 2). This can be rationalized by a higher surface loading of electrochemically active diiron catalyst. Importantly, switching from homogeneous to heterogeneous electrocatalysis with the metallopolymer, resulted in a significant drop in overpotential requirement and increase in catalytic current (Table 2). This is expected as diffusion limitations of the catalyst are circumvented following the immobilization of the metallopolymer at the electrode,[44] and could also indicate improved electronic communication between the electrode surface and a large fraction of the catalytic sites. In contrast, the **2**/MWNT composite exhibited a notable cathodic shift in the onset potential of approximately 40–50 mV (*i.e.*, −0.37 V *vs.* RHE), along with a significantly lower current density of −8 ± 2 mA cm^{-2} at −0.6 V *vs.* RHE compared to the metallopolymers under equivalent conditions. The substantial enhancement in the activity of the metallopolymers, despite a lower loading of active sites by 5–8 times compared to that of complex **2** (as per loading from ICP-OES), emphasizes the crucial role of the outer coordination sphere provided by the polymeric scaffold (Fig. 2B, orange trace, Table 2).[44]

2.2.3. Bulk electrolysis coupled with gas chromatography. In order to characterize the stability of the metallopolymer-functionalized electrodes under catalytic conditions and to quantify the amount of H_2 produced over time, chronoamperometry measurements (CA) were performed with the **1a–c**/MWNT modified electrodes. The CA experiments were carried out in neutral aqueous media (0.2 M phosphate buffer, pH 7) and the applied potential was set to −0.49 V *vs.* RHE for 20 hours. In parallel, the produced H_2 gas was detected and quantified by connecting the working electrode compartment of

Table 2 Quantitative analysis of the CV data of metallopolymers collected under homogeneous and heterogeneous conditions shown in Fig. 2. All CVs were performed in 0.2 M phosphate buffer at pH 7. The standard deviations were calculated based on a minimum of three independent experiments

	Homogeneous condition		Heterogeneous condition		
Metallo polymer	Onset potential[a] (V *vs.* RHE)	Current density at −0.65 V *vs.* RHE[b] (mA cm^{-2})	Onset potential[a] (V *vs.* RHE)	Current density at −0.6 V *vs.* RHE (mA cm^{-2})	Loading as per electrochemistry (nmol cm^{-2})
1a	−0.34	−2.42	−0.32	−36 ± 1	3.7 ± 0.3
1b	−0.35	−1.55	−0.33	−28 ± 1	2.7 ± 0.4
1c	−0.36	−1.17	−0.33	−24 ± 2	2.3 ± 0.4
2	nd[c]	nd	−0.37	−8 ± 2	13.9 ± 0.6

[a] The onset potential is calculated as a potential where catalytic current deviates ~10% from the capacitive current of respective traces. [b] The standard deviations for homogeneous condition were marginal. [c] nd = not determined.

the electrochemical cell to an inline gas chromatography system (micro-GC).

At the beginning of the CA experiment, **1a**/MWNT showed an initial current density of -2.7 ± 0.2 mA cm^{-2} (at $t = 1$ min to minimize capacitive current contribution). The current density was found to decline to -0.3 ± 0.1 mA cm^{-2} during the initial six hours and then remained fairly stable, however quite close to the current obtained for bare MWNT (-0.17 mA cm^{-2}). This corresponds to retention of only 8 ± 1% of the initial current density (Fig. 3A, red trace, Table S5†). Increasing the pyrene content of the metallopolymer to ~2.3 mol%, resulted in a significant improvement in stability of the catalytic current. **1b**/MWNT showed an initial current density of -2.8 ± 0.1 mA cm^{-2}, comparable to **1a**/MWNT, which dropped to -0.66 ± 0.12 mA cm^{-2} during the initial three hours. Following this initial current loss, the current density remained stable and 24 ± 2% of the initial current density was retained after 20 hours of electrolysis (-0.65 ± 0.10 mA cm^{-2}). Further increase in pyrene content, up to 6.6 mol% (**1c**/MWNT) caused a substantial drop in initial activity to -0.9 ± 0.1 mA cm^{-2} (Fig. 3A, blue trace, Table S5†). The electrocatalytic activity of **1c**/MWNT then followed a similar trend to **1b**/MWNT with a steady decrease of current during the three first hours to then stabilize around -0.35 ± 0.08 mA cm^{-2}. Interestingly, this current could be retained for at least 20 hours, corresponding to 38 ± 13% of the initial current density (Fig. 3A, green trace, Table S5†). Thus, following an initial current loss during the first three hours, the current density was remarkably stable for **1b** and **1c**. Indeed, in the case of **1b** and **1c** about 90–95% of the current densities observed after three hours, were retained after 20 hours. This represents a substantial improvement from the recently studied metallopolymers by our group where stable catalytic activity could not be reached within 20 hours of CA.[44] CA of the **2**/MWNT exhibited an initial current density of -0.9 ± 0.1 mA cm^{-2} (at $t = 1$ min), gradually decreasing to -0.20 ± 0.01 mA cm^{-2} (very close to blank *i.e.* -0.17 mA cm^{-2}). Overall, retention of 22 ± 4% of the initial current density was noted after 20 hours of CA (Fig. 3A, orange trace, Table S5†). The Faradaic efficiencies were estimated between 98–100% for all **1a–c**, **2**/MWNT based electrodes. As a result, 30 ± 1, 54 ± 1, 35 ± 2 and 16 ± 1 μmol of H_2 corresponding to TON_{H_2} of $1.3 \pm 0.1 \times 10^4$, $3.8 \pm 0.3 \times 10^4$, $3.0 \pm 0.4 \times 10^4$ and $0.6 \pm 0.1 \times 10^3$ were estimated for **1a**, **1b**, **1c** and **2** respectively, after 20 hours of electrolysis (Fig. 3B, S25, Tables S5 and S6†). The corresponding turnover frequency (TOF_{H_2}) values, determined after the first hour of CA (reached the maximum value), were 0.8 ± 0.4, 0.95 ± 0.20 and 0.8 ± 0.2 for **1a**, **1b** and **1c**, respectively. In contrast, complex **2** reached a maximum TOF_{H_2} of 0.008 ± 0.001 s^{-1}, almost two orders lower than metallopolymers during CA. The TOF_{H_2} of the metallopolymers on longer time-scales can be found in the ESI† (Fig. S30 and Table S6†). It should be noted that the values of TON_{H_2} and TOF_{H_2} were estimated considering the total diiron active sites detected as per ICP-OES measurements and are thus most likely conservative.

In order to understand the loss of current, a *post-operando* analysis using CV, UV-vis and ICP–OES was performed on the catalysts-functionalized electrodes (Fig. S31–S33†). UV-vis spectra, collected for all catalysts following desorption from the MWNT film, showed negligible loss of pyrene after the electrolysis (Fig. S31†).[37,44] This observation again underscores the strength of pyrene as an anchoring group on MWNT, as observed before for related diiron complex[37] and closely related metallopolymers.[44] Conversely, CV traces recorded in aqueous media after 20 hours of electrolysis revealed 70–90% loss and almost complete loss of the catalytic current (at -0.49 V *vs.* RHE) for **1a–c**/MWNT and **2**/MWNT, respectively (Fig. S32†). ICP-OES measurements of the iron content evolution of **1b**/MWNT at different time points of the CA showed a continuous loss of the iron concentration on the electrode *i.e.*, ~12%, ~40%, ~70% loss compared with the initial concentration after 1, 3 and 20 hours of CA, respectively (Table S6†). Thus, the long-term stability of the **1a–c**/MWNT metallopolymers can be rationalized by the relatively high retention of Fe during extended electrolysis. Indeed, the apparent stability of the active

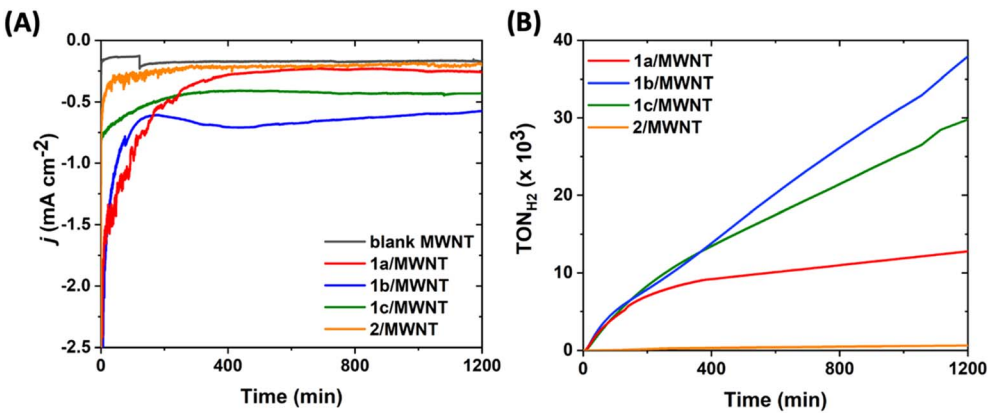

Fig. 3 CA of metallopolymers **1a–c** and complex **2** immobilized on MWNT/GCE. (A) Current density (*j*) *vs.* time; (B) turnover number (TON_{H_2}) *vs.* time recorded during CA at -0.49 V *vs.* RHE in 0.2 M sodium phosphate buffer, pH 7 under continuous flow of N_2 (5 mL min^{-1}). Here, bare MWNT, **1a**/MWNT, **1b**/MWNT, **1c**/MWNT and **2**/MWNT are represented by grey, red, blue, green and orange colors, respectively. The TON_{H_2} were calculated using loading from ICP-OES assessment.

sites is significantly improved in **1a–c**/MWNT when compared to the previously reported quinone-based [2Fe2S]-P(DMAEMA-*r*-PyBMA) (PyBMA = 4-(pyren-1-yl)-butyl methacrylate) metallopolymers.[44] Still, we note that the loss of current density of **1b**/MWNT only correlates weakly with the loss of Fe (Fig. S33 and Table S7†). The non-linear correlation between retained active sites (Fe ions) and activity again suggests the presence of different catalyst populations showcasing slightly different activities, where a relatively small fraction of highly active catalytic sites is lost relatively rapidly while slower but more robust catalysts remain active for several hours of electrolysis. The latter likely corresponds to a population of catalyst more deeply confined within the porous MWNT network or the polymer matrix bearing the active centre(s). The stable catalytic current are observed after three hours of CA could be attributed to the presence of (a) relatively stable population(s) of active sites that are not detected using CV measurement. Transformation of the CV-detectable $[2Fe2S]^{adt}$ active sites to yield this second population of the active sites or to degraded products like metallic Fe, on an hour time-scale is unlikely to fully rationalize the observed currents, since **1a**/MWNT displays the highest initial Fe content but the lowest long term currents.

3. Conclusion

This study demonstrated that the $\{Fe_2(\mu\text{-adt})(CO)_6\}$ derivatives can be incorporated within synthetic macromolecular scaffolds using free radical polymerization to prepare original metallopolymers, or "synthetic hydrogenases" (**1a–c**) with $\{Fe_2(\mu\text{-adt})(CO)_6\}$ as active site. All studied metallopolymers were active for H_2 production at neutral pH both under homogeneous and heterogeneous conditions. The long-term stability and H_2 production activity of the surface immobilized metallopolymers were found to correlate with pyrene content, with the best performing metallopolymer, **1b** (~2.3 mol% of pyrene), which could reach a TON_{H_2} of $3.8 \pm 0.3 \times 10^4$ (estimated from loading as per ICP-OES) within 20 hours of CA at neutral pH, with a Faradaic efficiency close to unity. Increasing the pyrene content further, as in **1c** (~6.6 mol% of pyrene), improved the durability but at the expense of current densities relative to **1b**. The drop in activity with increasing amount of pyrene from could not be solely attributed to the catalyst loading. This is in good agreement with the notion that pyrene, albeit important for stability, also introduces hydrophobicity to the metallopolymers which decreases H^+ diffusion to the catalytic sites.[44] Furthermore, the comparison of the activity of the metallopolymers to that of an isolated diiron site (complex **2**) allowed to confirm that the polymeric scaffold plays a crucial role in the catalytic process, enabling to reach TON values of about two orders of magnitude higher.[42] This allows to decipher the role of each amine of the adt^{2-} and DMAEMA amine, where adt^{2-} is unlikely to act as a direct proton-shuttle to the Fe ions during hydride formation. In the case of the metallopolymers studied here, any protonation must occur after the injection of at least one-electron into the system, as evident from the titration of **1b**.

Electrochemical experiments of the metallopolymers hinted towards the presence of at least two populations of active sites that likely differ *via* the nature of their electrostatic coupling with the electrode surfaces, arguably due to their various degree of confinement within the polymer matrix or the MWNT film. All metallopolymers display a rapid decrease of current density during the first hours, likely due to degradation of a more bulk exposed CV-detectable $[2Fe2S]^{adt}$ active site population. Still, for **1b** and **1c** the current density remains stable from three hours until the end of the CA experiment. This observation along with the ICP-OES measurements suggest the existence of a variety of population of active sites with long-term stability and lesser activity within the porous MWNT electrodes.

In closing, additional efforts are clearly required to increase the stability of the catalytic units as well as their relative polymer content. In parallel, efforts need to be invested in increasing the surface loading and stability of the polymers on the electrode surface, as the observed currents are still in the low mA range. Finally, we note that the outlined synthesis strategy paves the way for functionalization with a broad range of (organometallic) active sites to support other relevant energy conversion reactions.

Conflicts of interest

There are no conflicts to declare.

Acknowledgements

This work received funding from the French National Research Agency (Labex ARCANE, CBH-EUR-GS, ANR-17-EURE-0003), the European Union's Horizon 2020 Research and Innovation program under grant agreement no. 765376 (ESCALED Marie Curie ITN project), the Swedish Research Council (VR, 2021-04471) and the Swedish Energy Agency (STEM, 48574-1). We also acknowledge support of Pierre Marcasuzaa from UPPA and Cyril Colas from the "Fédération de Recherche ICOA/CBM (FR2708)" for the support regarding Size exclusion chromatography and High-resolution/accurate mass measurements (HRAM), respectively.

References

1 K. Bareiß, C. de la Rua, M. Möckl and T. Hamacher, Life Cycle Assessment of Hydrogen from Proton Exchange Membrane Water Electrolysis in Future Energy Systems, *Appl. Energy*, 2019, **237**, 862–872, DOI: **10.1016/j.apenergy.2019.01.001**.

2 M. Carmo, D. L. Fritz, J. Mergel and D. Stolten, A Comprehensive Review on PEM Water Electrolysis, *Int. J. Hydrogen Energy*, 2013, **38**(12), 4901–4934, DOI: **10.1016/j.ijhydene.2013.01.151**.

3 M. David, C. Ocampo-Martínez and R. Sánchez-Peña, Advances in Alkaline Water Electrolyzers: A Review, *J. Energy Storage*, 2019, **23**(2018), 392–403, DOI: **10.1016/j.est.2019.03.001**.

4 C. C. L. McCrory, S. Jung, I. M. Ferrer, S. M. Chatman, J. C. Peters and T. F. Jaramillo, Benchmarking Hydrogen Evolving Reaction and Oxygen Evolving Reaction

Electrocatalysts for Solar Water Splitting Devices, *J. Am. Chem. Soc.*, 2015, **137**(13), 4347–4357, DOI: 10.1021/ja510442p.

5 J. R. McKone, S. C. Marinescu, B. S. Brunschwig, J. R. Winkler and H. B. Gray, Earth-Abundant Hydrogen Evolution Electrocatalysts, *Chem. Sci.*, 2014, **5**(3), 865–878, DOI: 10.1039/C3SC51711J.

6 G. Segev, J. Kibsgaard, C. Hahn, Z. J. Xu, W.-H. Cheng (Sophia), T. G. Deutsch, C. Xiang, J. Z. Zhang, L. Hammarström, D. G. Nocera, A. Z. Weber, P. Agbo, T. Hisatomi, F. E. Osterloh, K. Domen, F. F. Abdi, S. Haussener, D. J. Miller, S. Ardo, P. C. McIntyre, T. Hannappel, S. Hu, H. Atwater, J. M. Gregoire, M. Z. Ertem, I. D. Sharp, K.-S. Choi, J. S. Lee, O. Ishitani, J. W. Ager, R. R. Prabhakar, A. T. Bell, S. W. Boettcher, K. Vincent, K. Takanabe, V. Artero, R. Napier, B. R. Cuenya, M. T. M. Koper, R. Van De Krol and F. Houle, The 2022 Solar Fuels Roadmap, *J. Phys. D: Appl. Phys.*, 2022, **55**(32), 323003, DOI: 10.1088/1361-6463/ac6f97.

7 J. T. Kleinhaus, F. Wittkamp, S. Yadav, D. Siegmund and U.-P. Apfel, [FeFe]-Hydrogenases: Maturation and Reactivity of Enzymatic Systems and Overview of Biomimetic Models, *Chem. Soc. Rev.*, 2021, **50**(3), 1668–1784, DOI: 10.1039/D0CS01089H.

8 H. Land, M. Senger, G. Berggren and S. T. Stripp, Current State of [FeFe]-Hydrogenase Research: Biodiversity and Spectroscopic Investigations, *ACS Catal.*, 2020, **10**(13), 7069–7086, DOI: 10.1021/acscatal.0c01614.

9 J. Esselborn, N. Muraki, K. Klein, V. Engelbrecht, N. Metzler-Nolte, U.-P. Apfel, E. Hofmann, G. Kurisu and T. Happe, A Structural View of Synthetic Cofactor Integration into [FeFe]-Hydrogenases, *Chem. Sci.*, 2016, **7**(2), 959–968, DOI: 10.1039/C5SC03397G.

10 Y. Nicolet, C. Piras, P. Legrand, C. E. Hatchikian and J. C. Fontecilla-Camps, Desulfovibrio Desulfuricans Iron Hydrogenase: The Structure Shows Unusual Coordination to an Active Site Fe Binuclear Center, *Structure*, 1999, **7**(1), 13–23, DOI: 10.1016/S0969-2126(99)80005-7.

11 J. W. Peters, X-Ray Crystal Structure of the Fe-Only Hydrogenase (CpI) from Clostridium Pasteurianum to 1.8 Angstrom Resolution, *Science*, 1998, **282**(5395), 1853–1858, DOI: 10.1126/science.282.5395.1853.

12 G. Berggren, A. Adamska, C. Lambertz, T. R. Simmons, J. Esselborn, M. Atta, S. Gambarelli, J.-M. Mouesca, E. Reijerse, W. Lubitz, T. Happe, V. Artero and M. Fontecave, Biomimetic Assembly and Activation of [FeFe]-Hydrogenases, *Nature*, 2013, **499**(7456), 66–69, DOI: 10.1038/nature12239.

13 J. A. Birrell, V. Pelmenschikov, N. Mishra, H. Wang, Y. Yoda, K. Tamasaku, T. B. Rauchfuss, S. P. Cramer, W. Lubitz and S. DeBeer, Spectroscopic and Computational Evidence That [FeFe] Hydrogenases Operate Exclusively with CO-Bridged Intermediates, *J. Am. Chem. Soc.*, 2020, **142**(1), 222–232, DOI: 10.1021/jacs.9b09745.

14 M. Sensi, M. del Barrio, C. Baffert, V. Fourmond and C. Léger, New Perspectives in Hydrogenase Direct Electrochemistry, *Curr. Opin. Electrochem.*, 2017, **5**(1), 135–145, DOI: 10.1016/j.coelec.2017.08.005.

15 V. Hitaishi, R. Clement, N. Bourassin, M. Baaden, A. De Poulpiquet, S. Sacquin-Mora, A. Ciaccafava and E. Lojou, Controlling Redox Enzyme Orientation at Planar Electrodes, *Catalysts*, 2018, **8**(5), 192, DOI: 10.3390/catal8050192.

16 E. Lojou, Hydrogenases as Catalysts for Fuel Cells: Strategies for Efficient Immobilization at Electrode Interfaces, *Electrochim. Acta*, 2011, **56**(28), 10385–10397, DOI: 10.1016/j.electacta.2011.03.002.

17 J. A. Laureanti, M. O'Hagan and W. J. Shaw, Chicken Fat for Catalysis: A Scaffold Is as Important for Molecular Complexes for Energy Transformations as It Is for Enzymes in Catalytic Function, *Sustainable Energy Fuels*, 2019, **3**(12), 3260–3278, DOI: 10.1039/C9SE00229D.

18 C. Esmieu, P. Raleiras and G. Berggren, From Protein Engineering to Artificial Enzymes – Biological and Biomimetic Approaches towards Sustainable Hydrogen Production, *Sustainable Energy Fuels*, 2018, **2**(4), 724–750, DOI: 10.1039/C7SE00582B.

19 A. C. Ghosh, C. Duboc and M. Gennari, Synergy between Metals for Small Molecule Activation: Enzymes and Bio-Inspired Complexes, *Coord. Chem. Rev.*, 2021, **428**, 213606, DOI: 10.1016/j.ccr.2020.213606.

20 B. Kandemir, S. Chakraborty, Y. Guo and K. L. Bren, Semisynthetic and Biomolecular Hydrogen Evolution Catalysts, *Inorg. Chem.*, 2016, **55**(2), 467–477, DOI: 10.1021/acs.inorgchem.5b02054.

21 D. Schilter, J. M. Camara, M. T. Huynh, S. Hammes-Schiffer and T. B. Rauchfuss, Hydrogenase Enzymes and Their Synthetic Models: The Role of Metal Hydrides, *Chem. Rev.*, 2016, **116**(15), 8693–8749, DOI: 10.1021/acs.chemrev.6b00180.

22 L. Sun, C. Duboc and K. Shen, Bioinspired Molecular Electrocatalysts for H_2 Production: Chemical Strategies, *ACS Catal.*, 2022, 9159–9170, DOI: 10.1021/acscatal.2c02171.

23 G. A. N. Felton, C. A. Mebi, B. J. Petro, A. K. Vannucci, D. H. Evans, R. S. Glass and D. L. Lichtenberger, Review of Electrochemical Studies of Complexes Containing the Fe2S2 Core Characteristic of [FeFe]-Hydrogenases Including Catalysis by These Complexes of the Reduction of Acids to Form Dihydrogen, *J. Organomet. Chem.*, 2009, **694**(17), 2681–2699, DOI: 10.1016/j.jorganchem.2009.03.017.

24 C. M. Thomas, O. Rüdiger, T. Liu, C. E. Carson, M. B. Hall and M. Y. Darensbourg, Synthesis of Carboxylic Acid-Modified [FeFe]-Hydrogenase Model Complexes Amenable to Surface Immobilization, *Organometallics*, 2007, **26**(16), 3976–3984, DOI: 10.1021/om7003354.

25 K. N. Green, J. L. Hess, C. M. Thomas and M. Y. Darensbourg, Resin-Bound Models of the [FeFe]-Hydrogenase Enzyme Active Site and Studies of Their Reactivity, *Dalton Trans.*, 2009, **22**, 4344–4350, DOI: 10.1039/B823152D.

26 V. Vijaikanth, J.-F. Capon, F. Gloaguen, P. Schollhammer and J. Talarmin, Chemically Modified Electrode Based on an Organometallic Model of the [FeFe] Hydrogenase Active

Center, *Electrochem. Commun.*, 2005, **7**(4), 427–430, DOI: 10.1016/j.elecom.2005.02.019.

27 A. Le Goff, V. Artero, R. Metayé, F. Moggia, B. Jousselme, M. Razavet, P. D. Tran, S. Palacin and M. Fontecave, Immobilization of FeFe Hydrogenase Mimics onto Carbon and Gold Electrodes by Controlled Aryldiazonium Salt Reduction: An Electrochemical, XPS and ATR-IR Study, *Int. J. Hydrogen Energy*, 2010, **35**(19), 10790–10796, DOI: 10.1016/j.ijhydene.2010.02.112.

28 S. K. Ibrahim, X. Liu, C. Tard and C. J. Pickett, Electropolymeric Materials Incorporating Subsite Structures Related to Iron-Only Hydrogenase: Active Ester Functionalised Poly(Pyrroles) for Covalent Binding of {2Fe3S}-Carbonyl/Cyanide Assemblies, *Chem. Commun.*, 2007, **15**, 1535, DOI: 10.1039/b617399c.

29 E. Xu, Z. Xiao, H. Liu, L. Long, L. Li and X. Liu, [FeFe]-Hydrogenase-Inspired Membrane Electrode and Its Catalytic Evolution of Hydrogen in Water, *RSC Adv.*, 2012, **2**(27), 10171, DOI: 10.1039/c2ra21036c.

30 L. Wang, Z. Xiao, X. Ru and X. Liu, Enable PVC Plastic for a Novel Role: Its Functionalisation with Diiron Models of the Sub-Unit of [FeFe]–Hydrogenase, Assembly of Film Electrodes, and Electrochemical Investigations, *RSC Adv.*, 2011, **1**(7), 1211, DOI: 10.1039/c1ra00343g.

31 X. Ru, X. Zeng, Z. Li, D. J. Evans, C. Zhan, Y. Tang, L. Wang and X. Liu, Bioinspired Polymer Functionalized with a Diiron Carbonyl Model Complex and Its Assembly onto the Surface of a Gold Electrode *via* "Click" Chemistry, *J. Polym. Sci., Part A: Polym. Chem.*, 2010, **48**(11), 2410–2417, DOI: 10.1002/pola.24010.

32 S. Dey, A. Rana, S. G. Dey and A. Dey, Electrochemical Hydrogen Production in Acidic Water by an Azadithiolate Bridged Synthetic Hydrogenese Mimic: Role of Aqueous Solvation in Lowering Overpotential, *ACS Catal.*, 2013, **3**(3), 429–436, DOI: 10.1021/cs300835a.

33 M. E. Ahmed, S. Dey, M. Y. Darensbourg and A. Dey, Oxygen-Tolerant H_2 Production by [FeFe]-H_2 Ase Active Site Mimics Aided by Second Sphere Proton Shuttle, *J. Am. Chem. Soc.*, 2018, **140**(39), 12457–12468, DOI: 10.1021/jacs.8b05983.

34 M. E. Ahmed, S. Dey, B. Mondal and A. Dey, H_2 Evolution Catalyzed by a FeFe-Hydrogenase Synthetic Model Covalently Attached to Graphite Surfaces, *Chem. Commun.*, 2017, **53**(58), 8188–8191, DOI: 10.1039/C7CC04281G.

35 M. E. Ahmed, A. Nayek, A. Križan, N. Coutard, A. Morozan, S. Ghosh Dey, R. Lomoth, L. Hammarström, V. Artero and A. Dey, A Bidirectional Bioinspired [FeFe]-Hydrogenase Model, *J. Am. Chem. Soc.*, 2022, **144**(8), 3614–3625, DOI: 10.1021/jacs.1c12605.

36 M. E. Ahmed, D. Saha, L. Wang, M. Gennari, S. Ghosh Dey, V. Artero, A. Dey and C. Duboc, An [FeFe]-Hydrogenase Mimic Immobilized through Simple Physiadsorption and Active for Aqueous H_2 Production, *ChemElectroChem*, 2021, **8**(9), 1674–1677, DOI: 10.1002/celc.202100377.

37 A. Zamader, B. Reuillard, J. Pécaut, L. Billon, A. Bousquet, G. Berggren and V. Artero, Non-Covalent Integration of a [FeFe]-Hydrogenase Mimic to Multiwalled Carbon Nanotubes for Electrocatalytic Hydrogen Evolution, *Chem.–Eur. J.*, 2022, **28**(69), e202202260, DOI: 10.1002/chem.202202260.

38 M. Karayilan, W. P. Brezinski, K. E. Clary, D. L. Lichtenberger, R. S. Glass and J. Pyun, Catalytic Metallopolymers from [2Fe–2S] Clusters: Artificial Metalloenzymes for Hydrogen Production, *Angew. Chem., Int. Ed.*, 2019, **58**(23), 7537–7550, DOI: 10.1002/anie.201813776.

39 F. Wang, W.-J. Liang, J.-X. Jian, C.-B. Li, B. Chen, C.-H. Tung and L.-Z. Wu, Exceptional Poly(Acrylic Acid)-Based Artificial [FeFe]-Hydrogenases for Photocatalytic H_2 Production in Water, *Angew. Chem.*, 2013, **125**(31), 8292–8296, DOI: 10.1002/ange.201303110.

40 M. Wen, X.-B. Li, J.-X. Jian, X.-Z. Wang, H.-L. Wu, B. Chen, C.-H. Tung and L.-Z. Wu, Secondary Coordination Sphere Accelerates Hole Transfer for Enhanced Hydrogen Photogeneration from [FeFe]-Hydrogenase Mimic and CdSe QDs in Water, *Sci. Rep.*, 2016, **6**(1), 29851, DOI: 10.1038/srep29851.

41 X. Zhu, W. Zhong and X. Liu, Polymers Functionalized with 1,2-Benzenedithiolate-Bridged Model Compound of [FeFe]-Hydrogenase: Synthesis, Characterization and Their Catalytic Activity, *Int. J. Hydrogen Energy*, 2016, **41**(32), 14068–14078, DOI: 10.1016/j.ijhydene.2016.06.025.

42 W. P. Brezinski, M. Karayilan, K. E. Clary, K. C. McCleary-Petersen, L. Fu, K. Matyjaszewski, D. H. Evans, D. L. Lichtenberger, R. S. Glass and J. Pyun, Macromolecular Engineering of the Outer Coordination Sphere of [2Fe-2S] Metallopolymers to Enhance Catalytic Activity for H_2 Production, *ACS Macro Lett.*, 2018, **7**(11), 1383–1387, DOI: 10.1021/acsmacrolett.8b00765.

43 W. P. Brezinski, M. Karayilan, K. E. Clary, N. G. Pavlopoulos, S. Li, L. Fu, K. Matyjaszewski, D. H. Evans, R. S. Glass, D. L. Lichtenberger and J. Pyun, [FeFe]-Hydrogenase Mimetic Metallopolymers with Enhanced Catalytic Activity for Hydrogen Production in Water, *Angew. Chem., Int. Ed.*, 2018, **57**(37), 11898–11902, DOI: 10.1002/anie.201804661.

44 A. Zamader, B. Reuillard, P. Marcasuzaa, A. Bousquet, L. Billon, J. J. Espí Gallart, G. Berggren and V. Artero, Electrode Integration of Synthetic Hydrogenase as Bioinspired and Noble Metal-Free Cathodes for Hydrogen Evolution, *ACS Catal.*, 2023, **13**, 1246–1256, DOI: 10.1021/acscatal.2c05175.

45 D. Heine, C. Pietsch, U. S. Schubert and W. Weigand, Controlled Radical Polymerization of Styrene-Based Models of the Active Site of the [FeFe]-Hydrogenase, *J. Polym. Sci. A Polym. Chem.*, 2013, **51**(10), 2171–2180, DOI: 10.1002/pola.26584.

46 A. Aster, S. Wang, M. Mirmohades, C. Esmieu, G. Berggren, L. Hammarström and R. Lomoth, Metal *vs.* Ligand Protonation and the Alleged Proton-Shuttling Role of the Azadithiolate Ligand in Catalytic H_2 Formation with FeFe Hydrogenase Model Complexes, *Chem. Sci.*, 2019, **10**(21), 5582–5588, DOI: 10.1039/C9SC00876D.

47 S. Dey, A. Rana, D. Crouthers, B. Mondal, P. K. Das, M. Y. Darensbourg and A. Dey, Electrocatalytic O_2 Reduction by [Fe–Fe]-Hydrogenase Active Site Models, *J.*

Am. Chem. Soc., 2014, **136**(25), 8847–8850, DOI: **10.1021/ja5021684**.

48 S. Tschierlei, S. Ott and R. Lomoth, Spectroscopically Characterized Intermediates of Catalytic H2 Formation by [FeFe] Hydrogenase Models, *Energy Environ. Sci.*, 2011, **4**(7), 2340, DOI: **10.1039/c0ee00708k**.

49 S. Ott, M. Kritikos, B. Åkermark, L. Sun and R. Lomoth, A Biomimetic Pathway for Hydrogen Evolution from a Model of the Iron Hydrogenase Active Site, *Angew. Chem.*, 2004, **116**(8), 1024–1027, DOI: **10.1002/ange.200353190**.

50 S. Jiang, J. Liu, Y. Shi, Z. Wang, B. Åkermark and L. Sun, Fe–S Complexes Containing Five-Membered Heterocycles: Novel Models for the Active Site of Hydrogenases with Unusual Low Reduction Potential, *Dalton Trans.*, 2007, **8**, 896–902, DOI: **10.1039/B615037C**.

51 A. J. Bard and L. R. Faulkner, *Electrochemical Methods: Fundamentals and Applications*, 2nd edn, Wiley, New York, 2001.

52 C. J. Kaminsky, S. Weng, J. Wright and Y. Surendranath, Adsorbed Cobalt Porphyrins Act like Metal Surfaces in Electrocatalysis, *Nat. Catal.*, 2022, **5**(5), 430–442, DOI: **10.1038/s41929-022-00791-6**.

53 J. Schild, B. Reuillard, A. Morozan, P. Chenevier, E. Gravel, E. Doris and V. Artero, Approaching Industrially Relevant Current Densities for Hydrogen Oxidation with a Bioinspired Molecular Catalytic Material, *J. Am. Chem. Soc.*, 2021, **143**(43), 18150–18158, DOI: **10.1021/jacs.1c07093**.

54 B. A. Johnson, A. M. Beiler, B. D. McCarthy and S. Ott, Transport Phenomena: Challenges and Opportunities for Molecular Catalysis in Metal–Organic Frameworks, *J. Am. Chem. Soc.*, 2020, **142**(28), 11941–11956, DOI: **10.1021/jacs.0c02899**.

